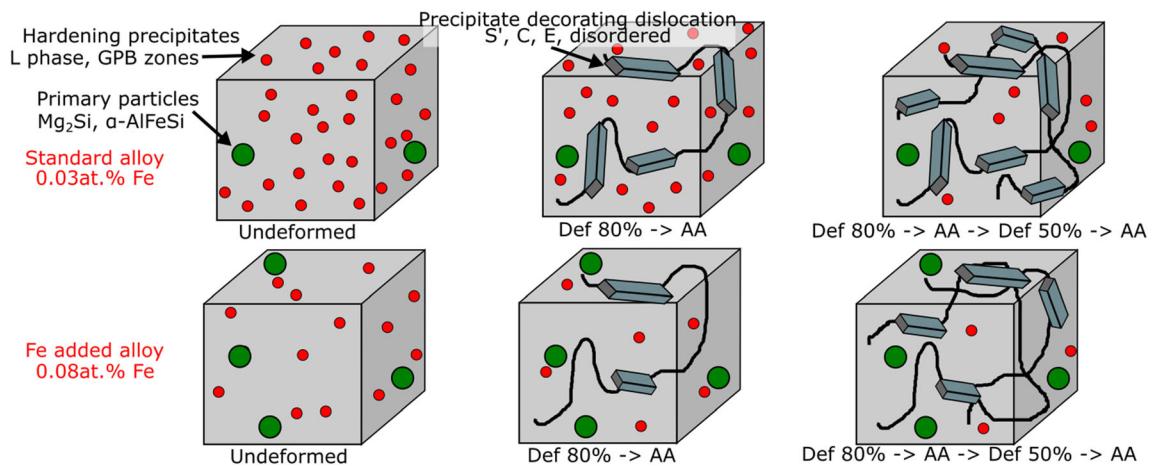


The Effect of Small Additions of Fe and Heavy Deformation on the Precipitation in an Al–1.1Mg–0.5Cu–0.3Si At. Pct Alloy



ELISABETH THRONSEN, HANNE MØRKESETH, CALIN D. MARIOARA, KAZUHIRO MINAKUCHI, TETSUYA KATSUMI, KNUT MARTHINSEN, KENJI MATSUDA, and RANDI HOLMESTAD

The effect of 0.03 and 0.08 at. pct Fe additions on the formation of secondary phases in an Al–1.1Mg–0.5Cu–0.3Si at. pct alloy was investigated. Following solution heat treatment and natural aging, the alloys were analyzed in an undeformed, artificially aged condition and in a two-step deformed condition consisting of 80 pct deformation, artificial aging, 50 pct deformation and a final, short artificial aging. Using electron microscopy, it was found that both alloys contained similar amounts of primary Mg_2Si particles, while the higher Fe level alloy produced roughly twice the number density and volume fraction of primary bcc α -AlFeSi particles. Lower volume fractions of hardening precipitates were measured in the high Fe level alloy, as attributed to the lower amount of Si available for precipitation. Using atomic resolution scanning transmission electron microscopy, a mix of L phases and structural elements of GPB zones was found in the undeformed conditions. In the deformed conditions, scanning precession electron diffraction revealed that the precipitates were nucleated both on and between deformation induced defects. The addition of Fe affected the relative ratio of these precipitates. Hardness measurements of conditions combining deformation and artificial aging were performed to investigate the hardening mechanisms at each processing step.



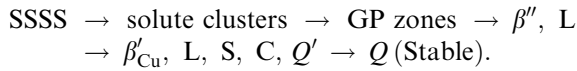
<https://doi.org/10.1007/s11661-022-06744-9>
© The Author(s) 2022

ELISABETH THRONSEN, HANNE MØRKESETH, RANDI HOLMESTAD are with the Department of Physics, Norwegian University of Science and Technology (NTNU), Høgskoleringen 5, 7491 Trondheim, Norway. Contact e-mail: Elisabeth.thronsen@ntnu.no CALIN D. MARIOARA is with the Materials and Nanotechnology Department, SINTEF Industry, Høgskoleringen 5, 7465 Trondheim, Norway. KAZUHIRO MINAKUCHI and TETSUYA KATSUMI are with the Machinery

and Engineering Group, YKK Corporation, 200, Yoshida, Kurobe, Toyama 938-8601, Japan. KNUT MARTHINSEN is with the Department of Materials Science and Engineering, NTNU, Sem Sælands veg 14, 7491 Trondheim, Norway. KENJI MATSUDA is with the Graduate School of Science and Engineering for Research, University of Toyama, Toyama 930-8555, Japan. Manuscript submitted January 8, 2022; accepted June 3, 2022.

I. INTRODUCTION

AGE-HARDENABLE Al–Mg–Si–Cu alloys exhibit a rapid hardening upon artificial aging (AA) at elevated temperatures. The increase in hardness is attributed to the formation of metastable, nano-sized precipitates which are (semi-)coherent with the Al-matrix. The amount and types of precipitates that form vary with the composition of the alloy and the thermomechanical treatment. The precipitation sequence in Al–Mg–Si–Cu alloys is normally given as^[1]:



SSSS is the supersaturated solid solution which forms when the alloy is quenched from a solution heat treatment (SHT) at temperatures above the solvus line (> 500 °C). For a thorough review of the different precipitate types and their characteristics, see our previous work.^[2–4] All metastable precipitates in the Al–Mg–Si(–Cu) system are needle/rod/lath shaped with main elongation parallel to the $\langle 100 \rangle_{\text{Al}}$ directions. They are structurally related through a common network of Si atomic columns along the precipitate lengths with a projected near hexagonal symmetry of 0.4 nm spacing.^[1,5,6] Different precipitate types can be distinguished by the atoms' position on the Si-network and the orientation of the network relative to the Al matrix. For the L- and C phases, the network is aligned along $\langle 100 \rangle_{\text{Al}}$, while for the β'' , β'_{Cu} , S and Q' , the network is aligned with $\langle 310 \rangle_{\text{Al}}$, $\langle 110 \rangle_{\text{Al}}$ and $\langle 510 \rangle_{\text{Al}}$.^[1] Al and Mg are always positioned in-between the Si-network columns, while Cu can either partly replace the Si columns (as in β'_{Cu})^[7] or be in-between them (as in Q' and C).^[2] Moreover, the crystal structures of these phases are governed by certain construction rules,^[8] which apply to the metastable precipitates in the Al–Mg–Cu and Al–Mg–Si(–Cu) systems. According to these rules, every Al atom has 12 nearest neighbors, every Mg atom has 15 and every Si or Cu has 9. This allows for atomic overlay of precipitates imaged in cross-section with the atomic-resolution high angle annular dark-field scanning transmission electron microscopy (HAADF-STEM) technique, because in projection every Al atom is surrounded by 4 atoms of opposite height, every Mg by 5 and every Si or Cu by 3.

Since all metastable phases in the precipitation sequence above have Mg/Si ratio ~ 1 . For alloys with excess Mg (Mg/Si > 1), the amount of Si in an alloy will be the limiting factor for the precipitation. In addition to participating in precipitation, Si contributes to the formation of primary particles such as Mg_2Si and various AlFeSi intermetallic compounds during solidification of the cast aluminum ingot. To minimize solute segregations, a homogenization treatment is normally performed. During this process, the Mg_2Si particles may dissolve.^[9] Fe has an almost negligible solubility in the Al matrix^[10] and contributes mainly to the formation of

non-soluble AlFeSi(Cu) particles during solidification. Thus, Fe is in general an unwanted element in Al alloys since such particles lower the material's ductility, in addition to lowering the hardening potential of the alloy as it leads to a reduced Si amount available for the formation of Al–Mg–Si(–Cu) hardening metastable phases. The needle- or plate like β -AlFeSi particles formed during solidification have been reported to transform to the more rounded body-centered cubic (bcc) or simple cubic (sc) α -AlFeSi particles during homogenisation.^[11] The bcc α -AlFeSi has composition close to $\text{Al}_{12}\text{Fe}_3\text{Si}$, while the β -AlFeSi composition is close to Al_5FeSi . The sc α -phase has a composition close to $\text{Al}_{13}\text{Fe}_3\text{Si}_{1.5}$.^[12] Even if Fe is unwanted in the alloy composition, it is usually hard to avoid since each processing step is a potential source for trace elements pick-up, such as Fe. For example, the bauxite itself contains Fe compounds.^[13] The increasing trend of using post-consumed Al-scrap also has the consequence of introducing impurity elements, like Fe. Understanding how Fe influences the microstructure and the final properties during different thermomechanical treatments is, therefore, important for further development of Al alloys in a recycling context.

In our previous work,^[4] (scanning) transmission electron microscopy (S)TEM and hardness measurements were used to investigate an Al–1.3Cu–1.0Mg–0.4Si wt pct alloy to understand the effect of heavy pre-deformation on the material. We showed that a pre-deformation of 80 pct changed the precipitate types that formed during a subsequent AA. In the undeformed AA sample, the microstructure consisted of L phases in addition to structural units of Guinier–Preston–Bagaryatsky (GPB) zones from the Al–Cu–Mg system.^[14,15] For the pre-deformed and AA samples, the L phase nucleated in the undistorted regions of the Al-matrix away from dislocations, while the C phase, S' phase and a newly discovered E phase^[4] nucleated on deformation-induced defects together with more disordered structures. This work is a continuation of the previous study, with two main objectives. First, and most important, is to investigate the effect of small additions of Fe on precipitation in both undeformed and heavily deformed conditions. The second is to investigate the effect on precipitation when additional deformation and artificial ageing steps are introduced, in the sequence SHT \rightarrow natural aging (NA) \rightarrow first deformation (Def1) \rightarrow artificial aging (AA1) \rightarrow second deformation (Def2) \rightarrow second artificial aging (AA2). This thermomechanical treatment is scientifically interesting due to the presence of precipitates prior to the second deformation process. There are two main types of precipitate-dislocation interactions: shearing and bypassing. Whether the microstructure of the material consists of shearable or non-shearable precipitates strongly affects the final properties. A fine, homogeneous distribution of shearable precipitates is usually associated with peak hardness in age-hardened materials, while non-shearable precipitates yield a higher

work-hardening potential. Precipitate type, size and morphology determine which of the two interactions dominate. Therefore, by investigating the characteristics of precipitates by scanning electron microscopy (SEM) and (S)TEM and the hardness evolution at each thermo-mechanical step, one can identify the processes taking place during the deformation.

II. EXPERIMENTAL PROCEDURE

A. Material and Heat Treatment

Two alloys were investigated in this work, one standard alloy (labelled as ‘Std’) and one with a small addition of Fe as compared to the standard (labelled as ‘Fe’). The measured compositions of the alloys are shown in Table I.

The alloys were cast, homogenized (505 °C, 3 hours) and extruded to a round profile (Ø 2.85 mm). The profiles were subjected to SHT at 505 °C for 3 hours and quenched to room temperature before they underwent NA for 18 hours. Subsequent to NA, the material underwent deformation Def1 (80 pct cold-rolling) and artificial aging AA1 (160 °C, 5 hours), deformation Def2 (50 pct cold-rolling) and AA2 (180 °C, 10 minutes). The thermomechanical treatment is indicated in Figure 1. In certain experiments, some of these steps were left out. The nomenclature for the different conditions is: Alloy_Def1,2_AA1,2, where ‘Alloy’ can be either Std

Table I. Measured Composition of the Two Alloys Investigated in the Present Work in Atomic Percent

Alloy	Cu	Mg	Si	Fe
Std	0.50 (1.17)	1.08 (0.97)	0.33 (0.34)	0.03 (0.07)
Fe	0.50 (1.17)	1.05 (0.94)	0.32 (0.34)	0.08 (0.16)

Weight percent is given in parenthesis.

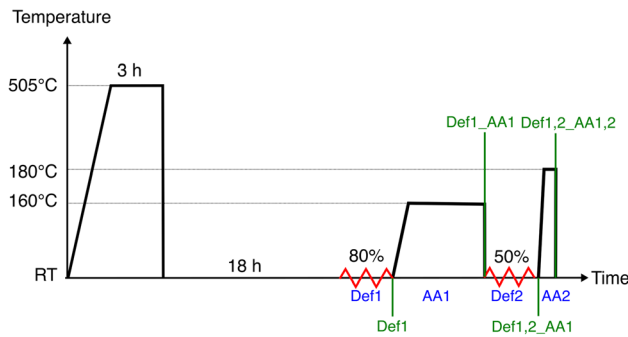


Fig. 1—The thermomechanical treatments the alloys were subjected to: Different combinations of Def1, AA1, Def2 and AA2 were executed to study different effects in the alloys. The nomenclature for the different processing routes is highlighted by the green text (Color figure online).

or Fe, indicating the standard- or Fe added alloy, respectively. *E.g.*, Std_Def1,2_AA1,2 is the standard alloy subjected to the full thermomechanical treatment shown in Figure 1. An overview over the different conditions and the techniques used to investigate them is shown in Table II. Both the Std- and Fe alloy were investigated for all conditions.

B. Vickers Hardness Test

An Innovatest Nova 360 micro-macro Vickers & Brinell hardness tester was used for hardness measurements. The load was 1 kgf and 7 indents were used per condition to get statistically reliable average hardness values.

C. EM Sample Preparation

1. SEM Sample Preparation

The samples were embedded in epoxy resin and then ground and polished followed by an active oxide polishing to a mirror-like surface. To avoid charging effects in the SEM, the epoxy resin was covered using Al foil and carbon tape.

2. TEM Sample Preparation

The samples were first mechanically polished to a thickness of 100 μm using a Struers Rotopol-21 before punched out to Ø3 mm disks. For the undeformed conditions (Alloy_AA1), the disks were punched out along the extrusion direction, while samples for the deformed conditions (Alloy_Def1,2_AA1,2, Alloy_Def1_AA1) were punched out from the surface perpendicular to the rolling- and extrusion direction. The samples were subsequently electropolished using a Struers TenuPol-5 twin-jet with an applied voltage of 20 V. The electrolyte consisted of 1/3 nitric acid and 2/3 methanol and was kept at $(-25 \pm 5)^\circ\text{C}$.

D. EM Studies

1. SEM Studies

Secondary electron (SE)- and backscattered electron (BSE) images and energy-dispersive X-ray spectroscopy (EDS) data were acquired using a Zeiss Ultra 55 SEM equipped with an EDS detector from Bruker. The settings used for the different modes in the SEM investigations are shown in Table III.

2. TEM Studies

A JEOL 2100 operated at a high voltage of 200 kV equipped with a Gatan GIF 2002 was used to acquire selected area electron diffraction (SAED) patterns, bright-field (BF)- and dark-field (DF) images. The acquisition of HAADF-STEM images was done in a double (image and probe) corrected JEOL ARM200F operated at 200 kV. The following parameters were used to obtain the images: 0.08 nm probe size, a convergence semi-angle of 27 mrad, and inner- and outer collection

Table II. The Different Conditions, Explanation of Their Thermomechanical Processing Route and the Techniques They Were Characterized By

	Processing Route	Hardness	TEM	SEM
AA1	AA1	x	x	x
Def1_AA1	Def1 → AA1	x	x	—
Def1,2_AA1,2	Def1 → AA1 → Def2 → AA2	x	x	—
Def1	Def1	x	—	—
Def1,2	Def1 → Def2	x	—	—
AA1,2	AA1 → AA2	x	—	—
Def1,2_AA1	Def1 → AA1 → Def2	x	—	—
Def1,2_AA2	Def1 → Def2 → AA2	x	—	—

Table III. Settings Used for the SEM Investigations

Operation Mode	SE	BSE	EDS
Acceleration Voltage	20 kV	10–12 kV	10–20 kV
Working Distance	10–25 mm	5–15 mm	5–10 mm
Current Mode	high current	high current	high current
Aperture Diameter	300 μm	120 μm	120/300 μm
Tilting Angle	0	0	0

Table IV. Chemical Composition and Lattice Parameter of the Unit Cell for the Different Phases Used for Estimating the Solute Balance

Particle/Precipitate	Composition	Unit cell lattice parameters	References
α -AlFeSi	$\text{Al}_{100}\text{Fe}_{24}\text{Si}_{14}$	Cubic, $a = 1.256 \text{ nm}$	21
Mg_2Si	Mg_8Si_4	Cubic, $a = 0.635 \text{ nm}$	22
L	$\text{Al}_{18.8}\text{Si}_{28.6}\text{Mg}_{36.9}\text{Cu}_{15.7}^*$	Monoclinic, $a = 1.032 \text{ nm}$, $b = 0.405 \text{ nm}$, $c = 0.810 \text{ nm}$, $\beta = 100.9^\circ$ **	2

*Result from the present work.
**C lattice parameter.

semi-angles 35 and 150 mrad, respectively. Before imaging precipitates, the specimen was tilted to a [001]Al zone axis. All HAADF-STEM images shown in this paper are filtered using a circular bandpass mask applied on the respective fast Fourier transform (FFT), and an inverse FFT (IFFT) performed on the masked area, suppressing all features with separation shorter than 0.15 nm in real space.

For the scanning precession electron diffraction (SPED) experiments, a JEOL 2100F operated at 200 kV and equipped with a Medipix3 MerlinEM camera with a single 256×256 Si chip from Quantum detectors was used.^[16] The instrument was operated in nanobeam electron diffraction mode using a convergence semi-angle of 1 mrad. The probe size was 1 nm, while the precession angle- and frequency was set to 8.7 mrad (= 0.5 deg) and 100 Hz, respectively. The double-rocking probe was aligned according to the approach described by Barnard *et al.*^[17] using the NanoMEGAS DigiSTAR control software. Diffraction patterns were recorded in the 12-bit mode of the Medipix3 detector using an exposure time of 40 ms. The step size was set to 1.3 nm and the scans comprised 400×400 pixels² (= 520×520 nm²)

E. EM Data Analysis

1. SEM Data Analysis

EDS data were analyzed with the Quantax Esprit software. Particles were analyzed using SE and BSE images. The image processing software Fiji^[18] was utilized to analyze the SE images, while the BSE images were analyzed using a Python script.^[19] Particle size, represented by the equivalent circle diameter (ECD), particle density and area fraction were obtained. For each sample, 10 to 12 images were analyzed, containing approximately 1300 particles.

2. TEM Data Analysis

a. Precipitate quantification Average precipitate length and cross-section were estimated based on BF images of the undeformed samples using the Fiji software. The number density and volume fractions were estimated using the approach given by Andersen.^[20] Estimations were based on 15 BF images for each of the undeformed samples (Alloy_AA1) yielding approximately 1500 counted precipitates per sample. The lengths were measured for 200 to 300 precipitates, while a total of

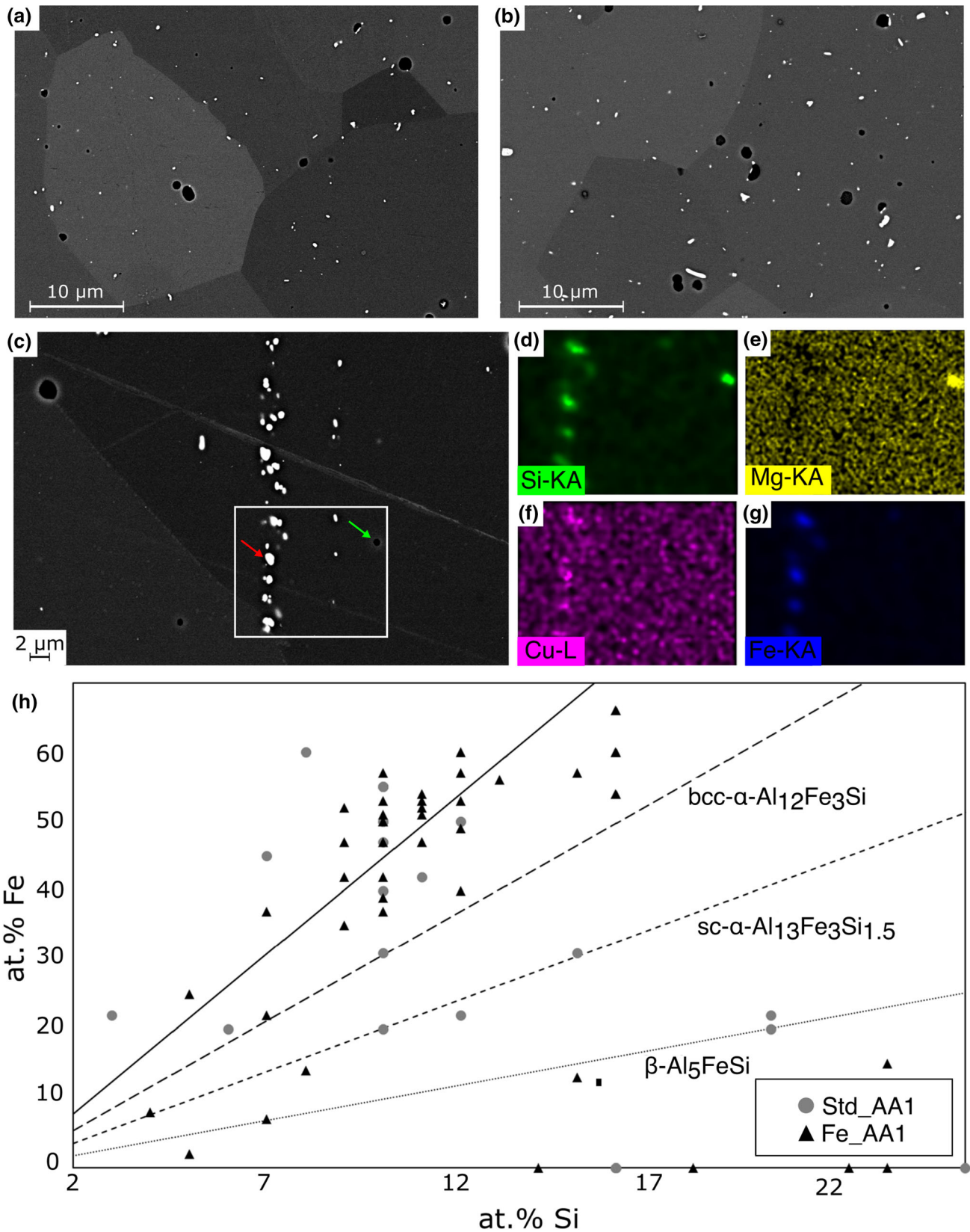


Fig. 2—(a) and (b) SEM BSE images showing two types of particles (bright and dark) in Std_AA1 and Fe_AA1, respectively. (c) BSE image from Std_AA1 and (d) through (g) corresponding EDS maps from the rectangle in (c) for Si, Mg, Cu and Fe, respectively. (h) Graph showing the concentration of Fe plotted against Si in the particles.

120 cross sectional areas from each sample were measured. Sample thickness was estimated based on electron energy loss spectroscopy (EELS). By multiplying the number density with the average precipitate length and cross section, the precipitate volume fraction, VF , was estimated.

b. Solute balance calculations The amount of solute locked up in each particle/precipitate type was calculated in the following way: The number of Al matrix atoms that would fit in the volume of a unit cell of a particle phase, N_{Al} was calculated. The number of solute atoms in one unit cell, N_{sol} is known from the chemical composition of the particle phase. Then, the solute fraction, SF, was calculated $SF = VF \cdot \frac{N_{sol}}{N_{Al}}$, where VF is the volume fraction of particles. The calculations were based on the compositions and lattice parameters in Table IV. The composition of the L phase is varying, and an average composition was estimated from the HAADF-STEM images. The L phase can be considered

a disordered version of the C phase, thus, the lattice parameters for C were used to calculate N_{Al} for L.

c. Overlay of HAADF-STEM images Two different approaches were used for the atomic overlay of HAADF-STEM images. Overlay was done based on the construction principles given by Andersen^[8] and explained in the Introduction of the current work: A column with nearest neighbors in fourfold-like symmetry was assumed to be Al, in fivefold-like symmetry Mg and in threefold-like symmetry Si or Cu. Further, Si and Cu were separated by the intensity: The Z-contrast of Cu ($Z_{Cu} = 29$) is much higher than that of Si ($Z_{Si} = 14$). Automatic overlay using the open-source software AutomAl6000^[23], based on the same principles, was used to analyze a large number of images in a shorter time than by manual overlay.

d. SPED data analysis The SPED data was processed using the open-source Python packages hyperspy,^[24]

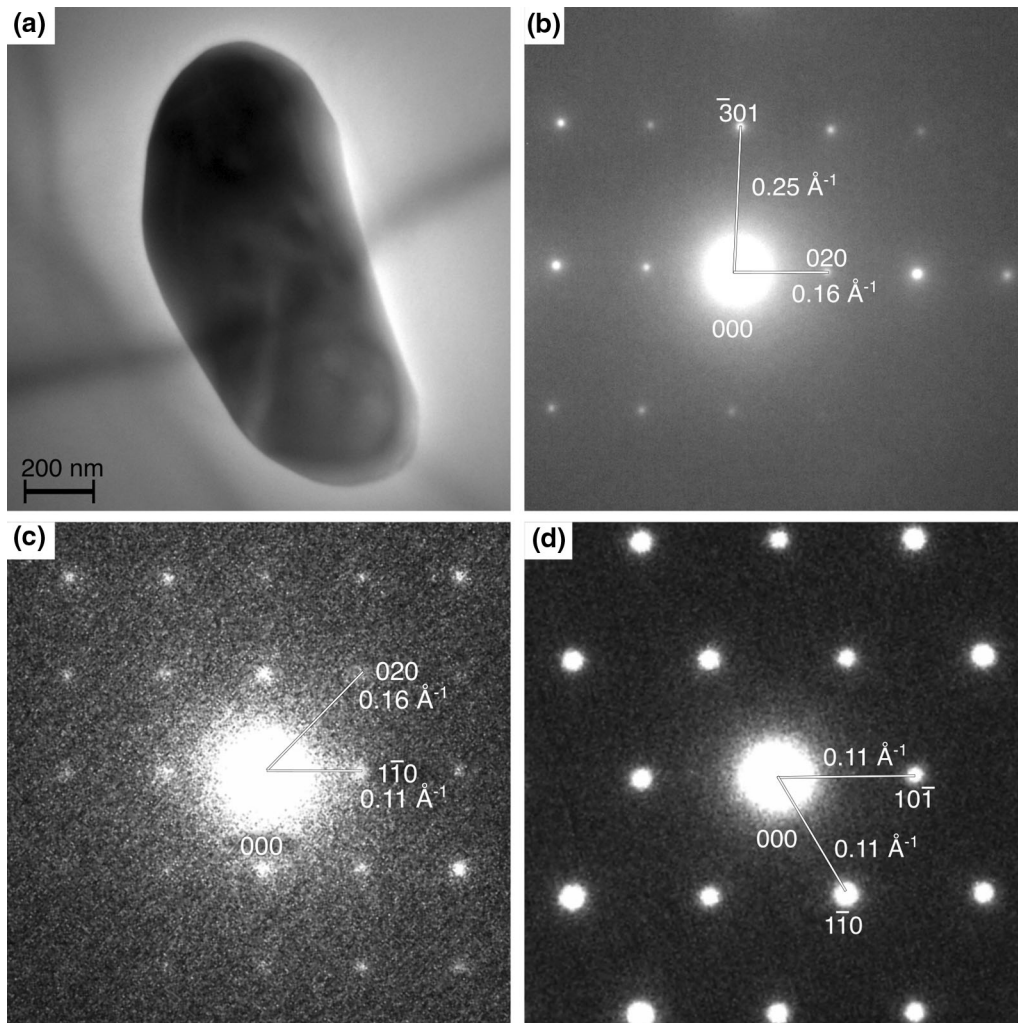


Fig. 3—TEM investigations of the AlFeSi(Cu) intermetallic compound found in both Std_AA1 and Fe_AA1. (a) A BF image of one representative particle. (b) through (d) SAED patterns from the [103]-, [001]-, and $\bar{1}\bar{1}1$ zone axes, respectively. The diffraction patterns in (b) and (c) are from the particle in a, while the one shown in (d) is from another AlFeSi(Cu)-particle. The lattice parameter was estimated to be 12.57, 12.61 and 12.57 Å based on the diffraction patterns in (b) through (d), respectively.

pyxem^[25] and scikit-image.^[26] To estimate the relative amounts of precipitates nucleated on dislocations to the ones nucleated in bulk the approach was as follows:

- i. A virtual aperture was placed in the obtained PED pattern stack and the image intensity within the aperture was integrated. The resulting image is a virtual dark-field (VDF) image.
- ii. The VDF images were background subtracted using a rolling ball correction,^[27] before they were thresholded using the triangle thresholding algorithm.^[28]
- iii. Each connected region in the VDF image was classified as a precipitate and categorized as nucleated on or between dislocations depending on its extent and Feret diameter.^[29]

To obtain phase maps and estimate the relative fraction of precipitates, a non-negative matrix factorization (NMF) decomposition^[30] was applied to the data. The approach is similar to the one presented in References 4 and 31 but with some alterations. A short summary is given in the following:

- i. Create masks in reciprocal space using blob-detection.
- ii. Superimpose the reciprocal space mask on the dataset and do NMF.
- iii. Manually label each NMF component into the following categories: C/L, S/E and disordered precipitates.
- iv. Based on the VDF image classification of precipitates, separate the L phases in bulk from the C- and L phases on dislocations. Do the same for the disordered precipitates.
- v. Calculate the area fraction of each of the five categories; C/L on dislocations, S/E on dislocations, disordered precipitates on dislocations, L in bulk and disordered in bulk, compared to the total area fraction of precipitates.

III. RESULTS AND DISCUSSIONS

A. Quantification of Primary Particles in the Undeformed Samples

Figure 2 shows the result from the SEM studies of primary particles in the Std- and Fe alloys in the AA1 condition. From the SEM BSE images in Figure 2(a) and (b), it is clear that two types of primary particles exist in this condition for both alloys. The first type appears dark in the BSE images and has a round morphology. The second type appears bright and is smaller than the dark ones. EDS was done to determine the composition of both types of particles. In Figure 2(c), a high magnification BSE image of Std_AA1 is shown. It is obtained normal to the extrusion direction and shows that the bright particles are aligned with the extrusion direction. Corresponding EDS maps for Si, Mg, Cu and Fe are shown in Figures 2(d) through (g), respectively, from the area marked by the white-line rectangle in Figure 2(c). One

white particle is indicated by the red arrow, and one dark particle by the green arrow. It is evident that the dark particles in the BSE images consist of Mg and Si, while the bright particles consist of Si, Fe and Cu. Based on this, the dark particles were assumed to be Mg₂Si and the bright particles AlFeSi(Cu) intermetallic compounds. EDS analyses of the Mg and Si-containing particles showed a varying Mg/Si ratio. In addition, some of the particles contained O. This is suspected to stem from dissolution of the Mg₂Si phase during polishing in water, which was done in preparation for both the SEM and the TEM specimens.^[32]

To further investigate the AlFeSi(Cu) intermetallic compounds, a total of 85 particles were analyzed. The concentration in atomic percent of Fe vs Si for the particles is shown in Figure 2(h). The three-dotted lines represent the expected compositions of β -AlFeSi, sc α -AlFeSi and bcc α -AlFeSi. It is noted that most of the analysed particles with bright contrast from both Std_AA1 and Fe_AA1 are composed of slightly less Si/Fe as compared to the expected lines of bcc α -AlFeSi. As indicated by Figure 2(f), this might be explained by some of the Cu substituting Si in the particles. This is not accounted for in our compositional analysis below since it is not clear to which extent this substitution takes place. Cu might also decorate the α -AlFeSi/Al interface, making it challenging to account for this when estimating the composition. The data points aligning along the x -axis in Figure 2(h) correspond to Mg₂Si particles.

TEM investigations of the AlFeSi(Cu) intermetallic particles by BF imaging and SAED were also conducted to investigate their identity. The results are shown in Figure 3. A BF image of a representative AlFeSi-particle from Std_AA1 is shown in (a). Figures 3(b) through (d) display SAED patterns from the [103]-, [001]-, and $\bar{1}11$ zone axis of AlFeSi(Cu) particles, respectively. The diffraction patterns in (b) and (c) are taken from the particle in a, while the one shown in d is from another particle. Based on these, the unit cell is indicated to be bcc with a lattice parameter between 12.57 and 12.61 Å, which compare well with the established value of 12.56 Å^[21] for bcc α -AlFeSi.

Density, area fraction and size of the primary particles were estimated based on images like the ones in Figures 2(a) and (b). The results are shown in Table V Results from SEM Image Analyses of Primary Particles. The particle size of α -AlFeSi is similar in both samples. The Mg₂Si particles are in general larger than the AlFeSi particles. Fe_AA1 contains about twice as many α -AlFeSi particles as Std_AA1, while the amount of Mg₂Si is comparable between the two alloys.

B. Precipitate Statistics for the Undeformed Samples

Two types of hardening precipitates with homogeneous distribution were found in the AA1 conditions of both Std- and Fe alloys, as shown in the BF images in Figures 4(a) and (b), respectively. The first precipitate type, indicated by yellow arrows, is lath-like with lath direction along (001)Al and its cross-section elongated

Table V. Results from SEM Image Analyses of Primary Particles

Sample	Density ($10^3/\text{mm}^2$)	Area Fraction (Pct)	Mean ECD (nm)
$\alpha\text{-AlFeSi}$			
Std_AA1	10.0 ± 2.3	0.31 ± 0.05	607 ± 93
Fe_AA1	21 ± 5.8	0.67 ± 0.12	600 ± 95
Mg_2Si			
Std_AA1	2.6 ± 1.4	0.40 ± 0.15	1515 ± 220
Fe_AA1	3.1 ± 1.1	0.44 ± 0.10	1028 ± 189

The average is the average of the corresponding quantity based on multiple images. The errors indicate the standard deviation of the estimated quantities between the analyzed images.

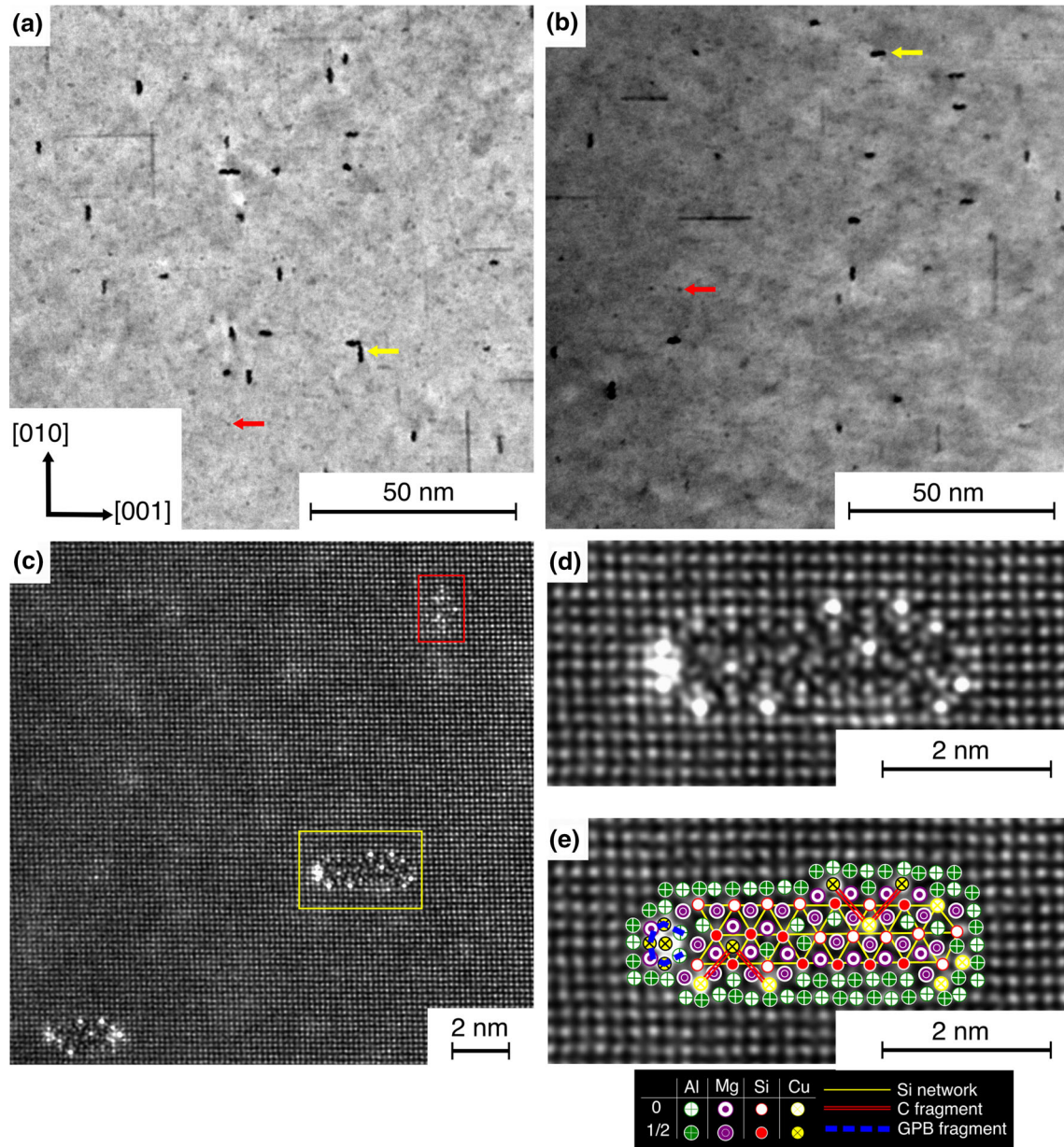


Fig. 4—(a) and (b) Overview BF images showing the existence of two precipitate types, indicated by yellow and red arrows in Std_AA1 and Fe_AA1, respectively. (c) HAADF-STEM image of Fe_AA1 showing the atomic structure of the precipitates. The yellow rectangle indicates the same precipitate as the yellow arrow in (a) and (b). This precipitate can be categorized as the L phase. The precipitate indicated by the red rectangle in c is the same type as the one indicated by red arrows in (a) and (b). It can be categorized as structural units of GPI zones. (d) Enlarged view of the L phase indicated by the yellow rectangle in (c). (e) Atomic overlay of the L phase in (d) (Color figure online).

along $\langle 100 \rangle$ Al. The second type, indicated by red arrows, is much smaller and has a rod morphology. HAADF-STEM images from the Fe_AA1 alloy like the one in Figure 4(c) revealed that the lath-like precipitates were L phases (exemplified by the yellow rectangle), while the rods were structural units of GPB zones (see for example the precipitate enclosed by the red rectangle). These are the same types of precipitates reported in our previous work on the Std alloy in the undeformed condition.^[4] To estimate the amount of Si locked in the precipitates in both samples, the average composition of the L phase was estimated from individual precipitates by overlaying HAADF-STEM images. An example is the L phase enclosed by the yellow rectangle in Figure 4(c). It is enlarged and overlaid in (d) and (e), respectively. For this individual precipitate, the composition was estimated to be $\text{Al}_{11}\text{Mg}_{34}\text{Si}_{23}\text{Cu}_{13}$. Based on HAADF-STEM images of 28 L precipitates, the average composition was estimated to be $\text{Al}_{18.8 \pm 3.3}\text{Mg}_{36.9 \pm 3.7}\text{Si}_{28.6 \pm 3.3}\text{Cu}_{15.7 \pm 3.8}$. We assume that the composition of the L phase is similar in the undeformed conditions of the Fe and Std alloy since their cross section is similar, see Table VI. The composition of the L phase has a slightly higher Mg/Si ratio than previously reported,^[33,34] but the higher Mg/Si ratio in the alloys studied in the present work may influence the Mg/Si ratio of the precipitates since the composition of the L phase is known to vary.^[2] Even if the L phase is overall disordered, it contains local C phase atomic configurations, indicated by the red lines in Figure 4(e). In addition, local symmetries seen in the GPB zones were often found at the ends of the precipitates, indicated by the blue dashed lines in (e). The exact same features were found in our previous work on the standard alloy in the undeformed condition.^[4]

The average length, cross section, number density and volume fraction of the L phase in Std_AA1 and Fe_AA1 are shown in Table VI. Due to the small size and weak intensity of the GPB zones (not to be confused with the GP zones in the Al–Mg–Si alloy system), these were not included in the precipitate statistics. However, this will not affect the estimation of Si locked up in precipitates, since GPB zones consist of Al, Cu and Mg.^[14,15] The cross section of the L phase is similar in the two alloys, Std_AA1 and Fe_AA1. The number density and volume fraction are lowest for Fe_AA1.

C. Solute Fraction

Based on the statistics from the primary particle- and precipitate analysis presented in Tables V and VI, respectively, and using the parameters listed in Table IV, the solute balance for each of the particle types was estimated, summed and compared to the composition of the alloys. The results are shown in Table VII. As discussed in the Introduction, the Si distribution is very important for the final microstructure of alloys with excess Mg.

It is evident that the primary particles and the L phase consume most of the Si from the alloy composition. This also validates our assumption that there is no significant incorporation of Si in GPB zones. It is also clear that the

higher amount of Fe in the Fe-added alloy results in more α -AlFeSi(Cu)-particles locking up Si, causing a lower amount of Si to be available for hardening phase precipitation as compared to Std_AA1. This explains the lower number density and volume fraction of the L phase in Fe_AA1 compared to Std_AA1. A consequence of this is that significant amounts of Mg and Cu are remaining and available for precipitation of clusters and GPB zones or they are simply left in solid solution in the matrix or aggregated on grain boundaries or other defects.

D. Precipitation in the Deformed Conditions

To investigate the precipitation in the Std- and Fe alloys in the deformed conditions, SPED and HAADF-STEM imaging were done. Due to the high density of dislocations, conventional TEM techniques gave unsatisfactory results as the contrast from the dislocations masked out the contrast from the precipitates. The chosen techniques also yield information on the precipitate type, not attainable from any conventional imaging technique.

Figure 5 shows VDF images for the Def1_AA1 condition for Std and Fe in (a) and (c), respectively. Figures 5(b) and (d) show VDF images for the Def1,2_AA1,2 condition for the Std and Fe alloy, respectively. The bright contrast stem from regions containing precipitates. It is assumed that all the elongated bright features arise from heterogeneous precipitation on deformation-induced defects, *e.g.* on dislocation lines or subgrain boundaries. Examples of such precipitates are highlighted with the pink arrows. In addition, precipitation also occurs homogeneously in the undistorted regions of the Al matrix, away from the deformation induced defects, exemplified by the yellow arrows. To get a more detailed insight into the effect of Fe on the precipitation in the deformed conditions, we aimed at differentiating between precipitates in the vicinity of deformation-induced defects compared to precipitation in the bulk. *I.e.*, quantification of the precipitates similar to the ones indicated by the pink arrows relative to the ones indicated by the yellow arrows in Figure 5. The approach is described in the Method section. In the following, the results for Def1_AA1 will be presented. For the Def1,2_AA1,2 condition, the microstructures for both alloys were too complex to be studied quantitatively. One challenge was the uneven background in the VDF images, evident in Figures 5(b) and (d). In addition, the PED patterns were less characteristic than in the Def1_AA1 condition, implying higher disorder in the precipitates in the Def1,2_AA1,2 condition. The SPED results from this condition will only be discussed qualitatively and phase identification using HAADF-STEM was performed.

Figure 6 shows the results from the precipitate quantification for Std_Def1_AA1 and Fe_Def1_AA1. The original VDF images are shown in (a) and (d), while (b) and (e) show the results from the quantification of precipitation on dislocations (pink) compared to precipitation in the bulk (yellow). All percentages are given as area fractions. The results imply that the addition of

Table VI. Precipitate Statistics for the L Phase in the Undeformed Samples

Sample	Length (nm)	Cross-Section (nm ²)	Number Density (μm^{-3})	Volume Fraction (Pct)
Std_AA1	18.6 ± 1.6	4.8 ± 2.1	78436 ± 12196	0.73 ± 0.13
Fe_AA1	13.4 ± 1.0	5.1 ± 1.8	50802 ± 5555	0.34 ± 0.03

For the cross-sections, the errors indicate the standard deviation between all individual measurements. The errors for the other values are the standard deviations between the 15 analyzed images.

Table VII. Solute Balance Showing the distribution of solute Between Primary Particles, L Phase and Al Matrix

Sample	Solute	α -AlFeSi(Cu)	Mg ₂ Si	L Phase	Sum	Alloy Composition
Std_AA1	Si	0.04	0.10	0.21	0.35	0.33
	Mg	—	0.21	0.27	0.48	1.08
	Fe	0.06	—	—	0.06	0.03
	Cu	—	—	0.11	0.11	0.50
Fe_AA1	Si	0.08	0.11	0.10	0.29	0.32
	Mg	—	0.23	0.12	0.35	1.05
	Fe	0.12	—	—	0.12	0.08
	Cu	—	—	0.05	0.05	0.50

All values are given in at. pct.

Fe causes a higher fraction of precipitation to occur on deformation-induced defects, since the relative area fraction of precipitation in bulk compared to on dislocations is 34 pct for the Fe alloy, as compared to 63 pct in the Std alloy.

The ordered, heterogeneously nucleated precipitates on dislocations were classified as E-, S', C- and L phases, while only the L phase and disordered structures were homogeneously nucleated in the bulk. This is in accordance with our previous work on the Std alloy in a condition similar to the Def1_AA1.^[4] The phase maps in Figures 6(c) and (f), for the Std- and Fe alloys, respectively, show that the same categories of precipitates were nucleated in both alloys. The precipitates are divided in five categories, based on their morphology and underlying PED pattern: Disordered precipitates, both on dislocations and in the bulk, L in bulk, E or S' on dislocations and C or L on dislocations. NMF was unsuccessful in differentiating between the S'- and E-phase, probably due to a combination of weak signal and similarity of the two patterns. Examples of PED patterns from the E- and S' phase are shown in Figures 6(g1) and (h1), respectively. FFTs of HAADF-STEM images of the E and S' phase are shown in Figures 6(g2) and (h2), there is a good correspondence between the FFTs and PED patterns of these precipitates. Since both precipitates also appear extended in the VDF images, they could not be separated. However, both the S'- and E phases nucleate on deformation induced defects, hence this challenge is not hindering the quantification of the relative amount of precipitation on deformation-induced defects compared to precipitation in the bulk. Examples of PED patterns originating from the L- and C phase are shown in Figures 6(i1) and (j1), respectively. The patterns are similar and could not be separated by the NMF decomposition. This is not unexpected: Both phases have habit plane [001]Al and

the L phase, although disordered, often contains local C symmetries. Based on their extent and the maximum Feret diameter,^[29] however, they could be separated during the postprocessing of the data.

To investigate which precipitate structures existed in the Def1,2_AA1,2 conditions, HAADF-STEM investigations were conducted to see the atomic structure of the precipitates. This was done for the Fe alloy. This was deemed sufficient, since there are clear indications that the addition of Fe does not affect which precipitate types nucleate, only their relative amounts. The results are shown in Figure 7. Both ordered and disordered precipitates were found. All the precipitates imaged were nucleated on dislocations. In a, an example of the C phase viewed along its [010] direction is shown. This was the most common type of ordered precipitates in this condition. The second type of ordered precipitate was the S' phase, an example is shown in (b). The S' phase is known to preferentially nucleate on dislocations.^[14] Most of the imaged precipitates, however, were disordered and these could be separated into three categories: (1) small, with well-defined cross-sections often containing local structural units of GPB zones, (2) hybrid Al-Mg-Si-Cu/Al-Mg-Cu precipitates and (3) large, disordered ones with wide cross sections. An example of the first category is shown in (c). The local GPB symmetry is indicated by the blue-dashed lines. In (d), an example of a hybrid precipitate is shown. It consists of four distinct regions, marked by numbers in the figure. The segment enclosed by region 1 is the C phase viewed along its [001] direction, while the segment in region 2 corresponds to the S' phase. In region 3, the only instance for which the E phase^[4] was found, is shown. The segment enclosed by region 4 is a disordered part of the structure. In Figure 7(e), a disordered precipitate with wide cross-section is shown.

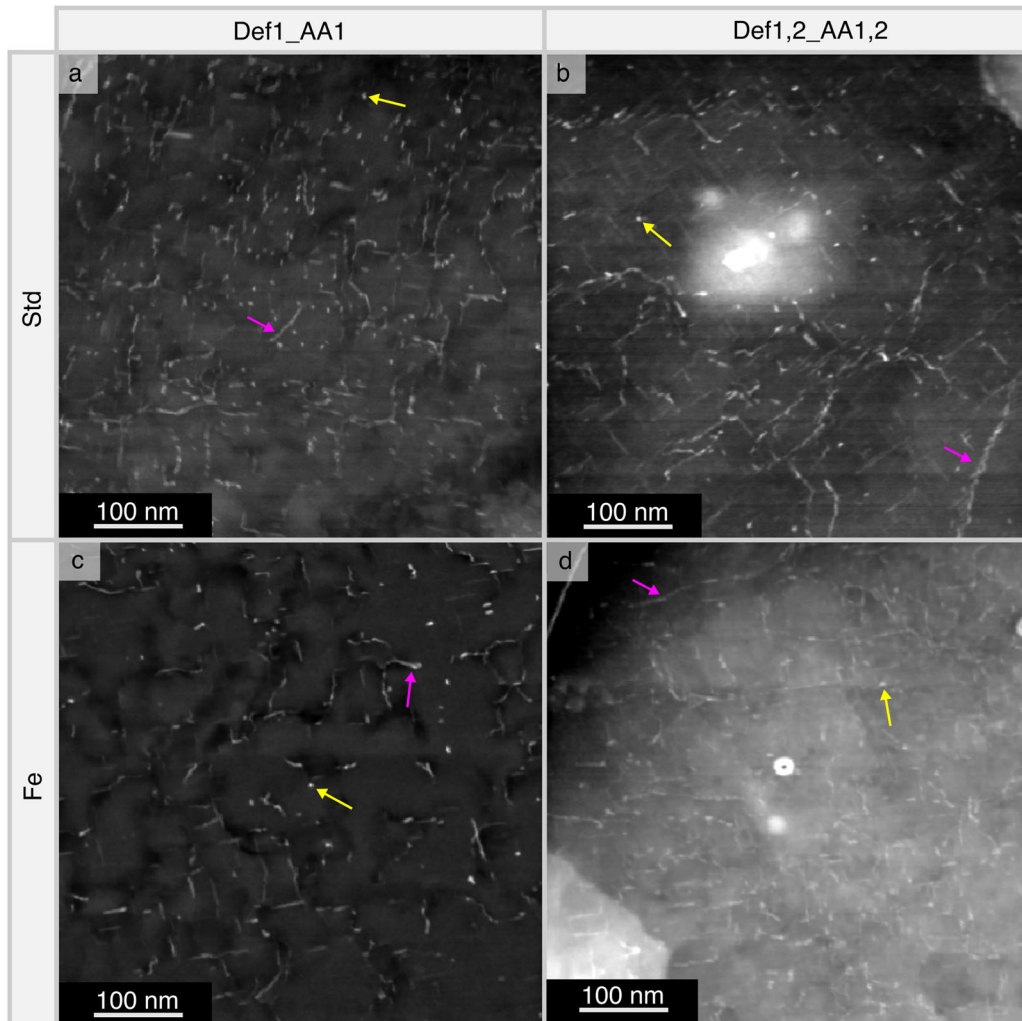


Fig. 5—VDF images of the deformed conditions Def1_AA1 (a, c) and Def1,2_AA1,2 (b, d) for the Std (top)- and Fe (bottom) alloys. The yellow- and pink arrows indicate precipitation between and on deformation-induced defects, respectively (Color figure online).

E. Hardness Evolution and Relation to Microstructure

In the following, an assessment of the different mechanisms involved during each thermomechanical step will be elaborated. The discussion will be based on the TEM data from the deformed conditions, hardness measurements, the amount of Si locked in primary particles and direct observations of precipitate number densities in the undeformed conditions.

The hardness in each processing step for three different thermomechanical treatments was measured. The different thermomechanical treatments were Def1,2_AA1,2, Def1,2_AA2 and AA1,2 and the results are shown in Figure for both the Std- and Fe alloy.

During NA, the increase in HV is slightly higher in the Std alloy most likely due to the higher amount of Si available for precipitation in this alloy. It is well known that Si contributes to the clustering of solute atoms during NA and that the NA hardness increases with increasing Si content.^[35] For the Def1,2_AA2 processing route shown in a and d for the Std- and Fe alloy, respectively, the Def1 and Def2 treatments yield similar increase in hardness. This indicates that the higher

cluster density in the Std alloy does not affect the build-up of dislocations. Hence, the clusters are most likely shearable. This is reasonable considering their very small size. AA2 yields a higher hardness increase in the Std alloy compared to the Fe alloy, probably due to a higher number density of hardening phases following the higher amount of Si available for precipitation. Note that the hardness increases are similar, indicating that the effect of the small addition of Fe is not considerably detrimental.

The hardness for the processing route without deformation (AA1,2) is shown in Figures 8(b) and (e) for the Std and Fe alloy, respectively. After AA1, the Std alloy is slightly harder than the Fe alloy. Since the L phase is considered the main hardening precipitate in these alloys, the difference in the ageing response in the two alloys is attributed to the higher number density of the L phase in the Std alloy compared to the Fe alloy in this condition, *c.f.* Table VI. However, the difference in ageing response is not substantial. Thus, small additions of Fe are not particularly detrimental to the hardness in the T6 condition. During AA2, the hardness of both

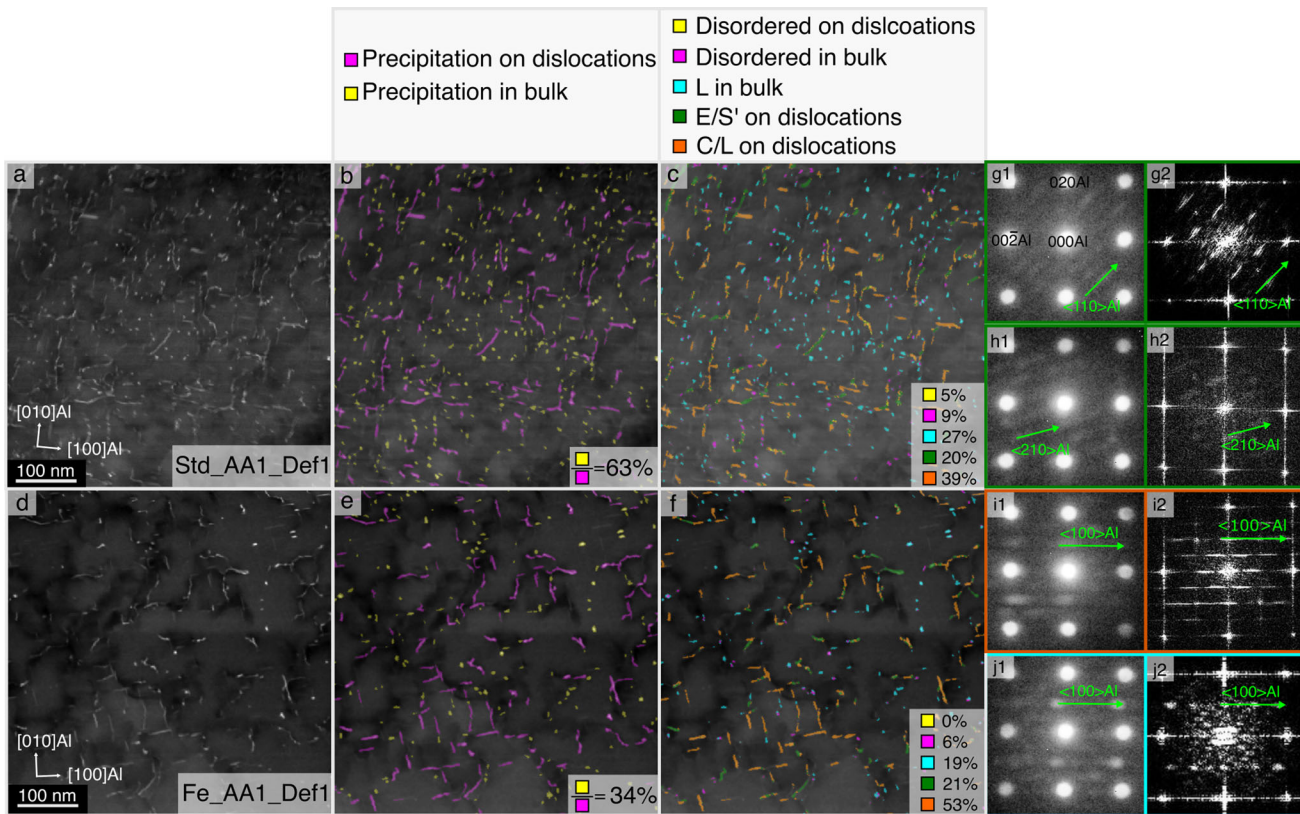


Fig. 6—Results from the quantification of precipitates in the AA1_Def1 condition. (a) and (d) VDF images from the Std- and Fe alloy, respectively. (b) and (e) Quantification of precipitates on deformation induced defects, such as dislocations, compared to precipitation in the bulk. (c) and (f) Phase mapping of the precipitates. (g1), (h1), (i1), (j1) Selected PED patterns from E-, S'-, C- and L phases, respectively. (g2), (h2), (i2), (j2): FFTs of E-, S-, C- and L phases, respectively. The FFTs in (g2), (i2) and (j2) is taken from Ref. [4], while (h2) is the FFT of Fig. 7(b). The colour scheme emphasizes how the different precipitates are categorized in the phase maps in (c) and (f) (Color figure online).

alloys decreases, indicating that the alloys are slightly overaged.

Hardness evolution for the Def1,2_AA1,2 processing route is shown in Figures 8(c) and (f) for the Std- and Fe alloy, respectively. The ageing response during AA1 in the pre-deformed condition is significantly reduced compared to the undeformed conditions as seen in Figures 8(b) and (e). This is attributed to the reduction of homogeneous nucleation due to the high density of dislocations in the AA1_Def1 condition. Due to the higher diffusivity at dislocations and the favorable nucleation conditions at deformation induced defects, the precipitates on dislocations are coarser compared to the homogeneously nucleated precipitates.^[36,37] It is evident from the phase maps in Figures 6(c) and (f) that the E-, S'- and C phases account for most of the precipitation on dislocations, while the homogeneously nucleated precipitates mostly consist of the L phase, which is also homogeneously nucleated in the undeformed samples, *c.f.* Figure 4.

The SPED data gave indications that the relative amount of homogeneous and heterogeneous nucleation differed in the two alloys, namely that the homogeneous nucleation was suppressed to a larger extent in the Fe alloy compared to the Std alloy. Teichmann *et al.*^[38] found that for an Al–Mg–Si alloy, no homogeneous nucleation took place during the early stages of ageing

of a 10 pct pre-deformed sample. For the same alloy and pre-deformation, the authors found a small fraction of hardening phases homogeneously nucleated in the microstructure after prolonged ageing.^[39] These observations confirm that the dislocations provide heterogeneous nucleation sites as well as changing the diffusivity by attracting vacancies, effectively changing the ageing kinetics. Solute atoms might also segregate at dislocations, creating a solute depleted region in the vicinity of the dislocations. Based on these observations, it is probable that the lower amount of Si available for precipitation in the Fe alloy leads to a higher fraction of heterogeneous precipitation compared to the Std alloy, since the dislocations can deplete the matrix both of solutes and vacancies. Homogeneous nucleation will be suppressed due to the fast nucleation of precipitates at the deformation-induced defects during the very early stages of AA and less Si will be available for homogeneous nucleation than in the Std alloy in the intermediate stages of AA. It is interesting to note that although there is a measurable microstructural difference in terms of precipitation between the alloys, the hardness response during AA1 after Def1 is similar between the two alloys. A material's hardness is its ability to resist deformation and is affected both by precipitates and dislocations. Based on our observations, it is probable that the heavy pre-deformation causes the contribution

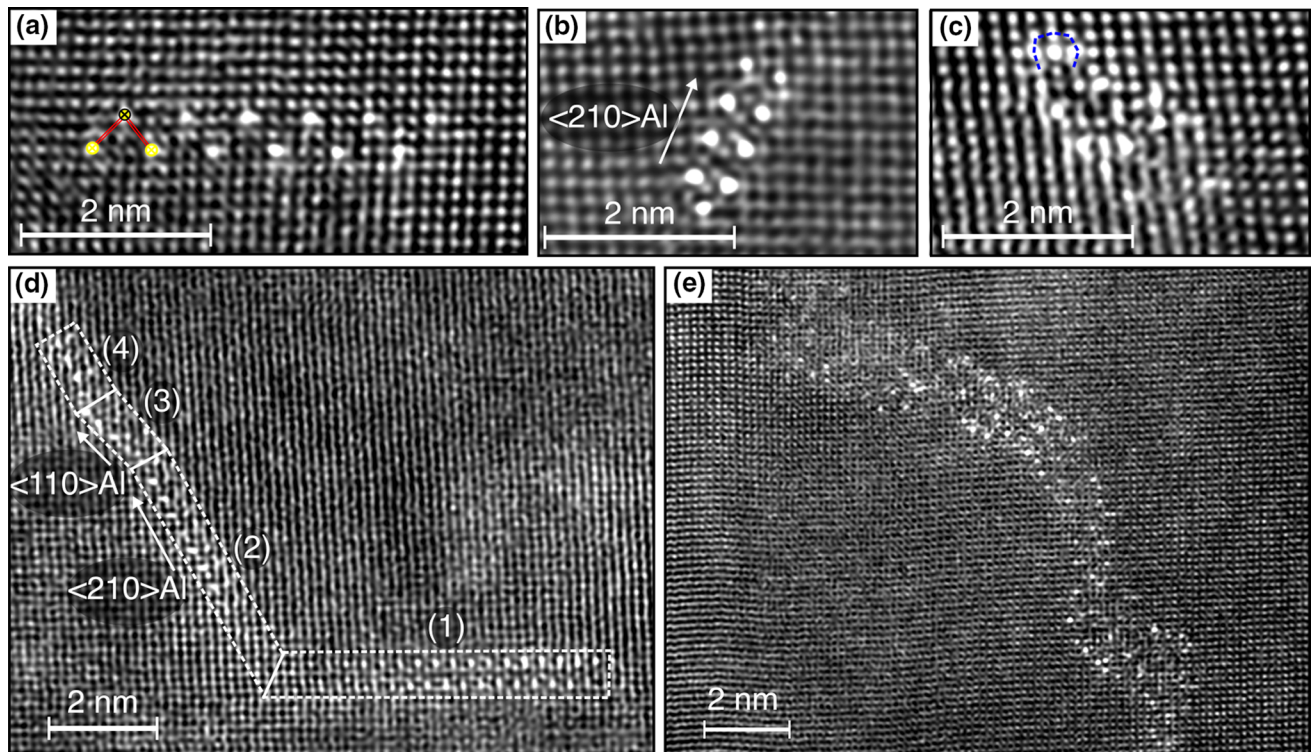


Fig. 7—HAADF-STEM images of the precipitates found in Fe_{Def1,2_AA1,2}. (a) C phase viewed along [010]C, its characteristic symmetry is indicated by the red lines. (b) S' phase from the Al–Cu–Mg system. (c) Disordered precipitate containing local GPB symmetries. (d) A hybrid precipitate containing the (1) C phase, (2) S' phase, (3) E phase and (4) disordering. (e) Disordered precipitate with wide cross-section (Color figure online).

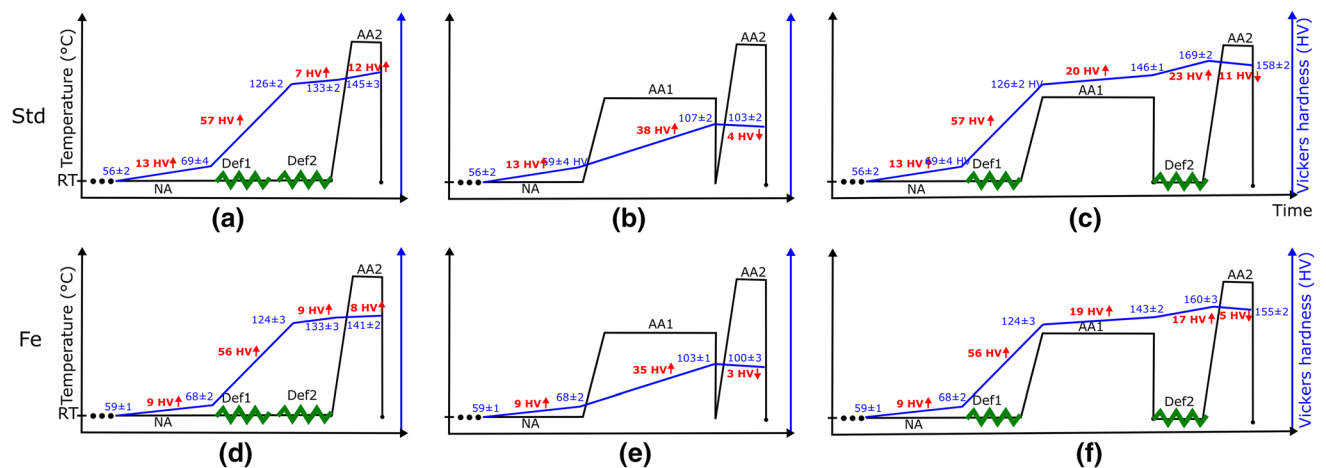


Fig. 8—Hardness evolution for the two alloys in each step for 3 different thermomechanical processing routes: Def1,2_AA2 (a) and (d), AA1,2 (b) and (e) and Def1,2_AA1,2 (c) and (f). The top row shows hardness for the Std alloy, while the bottom row shows hardness for the Fe alloy.

from the dislocations to the hardness to dominate compared to the differences observed in the precipitation. It is important to keep in mind that the precipitate fractions presented for the Def1_AA1 conditions are relative fractions, namely that we have not measured the absolute volume fractions of precipitates in the two alloys. It is, however, reasonable to assume that the volume fraction of precipitates is higher for the Std alloy than the Fe alloy, based on the precipitate statistics from the undeformed condition.

During the subsequent Def2 treatment following AA1_Def1, the hardness response is more prominent in the Std alloy compared to the Fe alloy. Since the hardness increase during Def2 was similar between the two alloys without AA1, see Figures 8(a) and (d), this must be attributed to a difference in the precipitate-dislocation interactions during deformation. Non-shearable precipitates are known to yield a higher work hardening due to the formation and storage of dislocation loops around the precipitates, effectively increasing

the dislocation density.^[40] This indicates that the Std alloy in the Def1_AA1 condition has a higher volume fraction of non-shearable precipitates than the Fe alloy. Assuming that the thicknesses of the regions in the VDF images in Figures 6(a) and (d) are similar, there is a larger fraction of precipitates nucleated in the Std alloy in this condition. This is a reasonable observation, since the α -AlFeSi(Cu) particles are unaffected by the deformation, effectively locking the same amount of Si solutes through all the processing steps.

Quantification of the microstructure in the AA1,2_Def1,2 condition was challenging, but qualitatively based on the HAADF-STEM observations exemplified in Figure 7 and VDF images in Figures 5(b) and (d), we conclude that the microstructure in this condition mostly consists of heterogeneously nucleated precipitates, while a small amount of the precipitates is nucleated in the undistorted regions of the Al matrix. As the hardness decreases for both alloys during AA2, this is attributed to the dissolution and transformation of the homogeneously nucleated precipitates to heterogeneously nucleated precipitates. It is unclear whether the transformation is induced by Def2 or AA2 or a combination of these two.

In undeformed materials, the amount of precipitates is very important for the material's final properties. In the present study, the higher amount of L phase in the Std_AA1 condition contributed to a higher peak hardness than in the Fe_AA1. If, however, the material was deformed prior to AA1, the hardness increase during AA1 was similar. We can therefore conclude that with pre-deformation, the effect of Fe will be less detrimental to the mechanical properties of the material. By doing a second deformation and AA treatment, Def2 and AA2, the detrimental effect of Fe on the mechanical properties is again increased, due to the lower amount of non-shearable precipitates nucleated on dislocations, yielding a lower work hardening response.

IV. CONCLUSIONS

In summary, this study has investigated the effect of small additions of Fe on precipitation in an undeformed, and a heavily deformed Al-Mg-Si-Cu alloy. The samples were deformed twice: One deformation treatment of 80 pct prior to AA for 5 hours at 160 °C was followed by a subsequent deformation of 50 pct and a second AA for 10 minutes at 180 °C to produce the final condition. The main findings include:

1. The microstructure of the undeformed samples consists of Mg₂Si- and α -AlFeSi primary particles, L phase and structural units of GPB zones. A higher amount of α -AlFeSi prevailed in the Fe added alloy decreasing the Si level available for the precipitation of hardening precipitates. The consequence was a lower number density and lower volume fraction of the L phase. This had a small, negative influence on the hardness of the Fe added alloy as compared to the standard alloy in the undeformed condition.

2. The addition of Fe affected the precipitation during artificial ageing after the first pre-deformation. The precipitation in the Fe alloy was more heterogeneous compared to the Std alloy. This was attributed to the lower amount of Si available for precipitation in this alloy. The precipitate types in the vicinity of deformation-induced defects were C-, E-, S' and disordered precipitates, while the precipitation in bulk was dominated by the L phase for both alloys.
3. The precipitate types in the final condition were the ordered C-, E- and S' phases and disordered structures.
4. The hardness increase during the second deformation is highest in the standard alloy, suggesting that this condition contains a higher fraction of non-shearable precipitates as compared to the Fe added alloy.

ACKNOWLEDGMENTS

This work was supported by the INTPART project 'Norwegian-Japanese Aluminium alloy Research and Education Collaboration Phase-2' (Grant Number 287965) financed by The Research Council of Norway (RCN). The (S)TEM work was carried out on the NORTEM (Grant Number 197405) infrastructure at the TEM Gemini Centre, Trondheim. E.T. and R.H. acknowledge the AllDesign project/NTNUs Digitalisation Initiative.

FUNDING

Open access funding provided by NTNU Norwegian University of Science and Technology (incl St. Olavs Hospital - Trondheim University Hospital).

DATA AVAILABILITY

The raw data required to reproduce these findings are available to download from <https://doi.org/10.5281/zenodo.5636674>.

CONFLICT OF INTEREST

On behalf of all authors, the corresponding author states that there is no conflict of interest.

OPEN ACCESS

This article is licensed under a Creative Commons Attribution 4.0 International License, which permits use, sharing, adaptation, distribution and reproduction in any medium or format, as long as you give appropriate credit to the original author(s) and the source,

provide a link to the Creative Commons licence, and indicate if changes were made. The images or other third party material in this article are included in the article's Creative Commons licence, unless indicated otherwise in a credit line to the material. If material is not included in the article's Creative Commons licence and your intended use is not permitted by statutory regulation or exceeds the permitted use, you will need to obtain permission directly from the copyright holder. To view a copy of this licence, visit <http://creativecommons.org/licenses/by/4.0/>.

REFERENCES

- C.D. Marioara, S.J. Andersen, T.N. Stene, H. Hasting, J. Walm-sley, A.T.J. van Helvoort, and R. Holmestad: *Philos. Mag.*, 2007, vol. 87, pp. 3385–413.
- T. Saito, E.A. Mørtzell, S. Wenner, C.D. Marioara, S.J. Andersen, J. Friis, K. Matsuda, and R. Holmestad: *Adv. Eng. Mater.*, 2018, vol. 20, p. 1800125.
- J.K. Sunde, C.D. Marioara, and R. Holmestad: *Mater. Charact.*, 2020, vol. 160, p. 110087.
- E. Thronsen, C.D. Marioara, J.K. Sunde, K. Minakuchi, T. Katsumi, I. Erga, S.J. Andersen, J. Friis, K. Marthinsen, K. Matsuda, and R. Holmestad: *Mater. Des.*, 2020, vol. 186, p. 108203.
- C. Cayron, L. Sagalowicz, L. Sagalowicz, and P.A. Buffat: *Philos Mag A*, 1999, vol. 79, pp. 2833–51.
- S.J. Andersen, C.D. Marioara, R. Vissers, A. Frøseth, and H.W. Zandbergen: *Mater. Sci. Eng. A*, 2007, vol. 444, pp. 157–69.
- T. Saito, C.D. Marioara, S.J. Andersen, W. Lefebvre, and R. Holmestad: *Philos. Mag.*, 2014, vol. 94, pp. 520–31.
- S.J. Andersen, C.D. Marioara, J. Friis, R. Bjørge, Q. Du, I.G. Ringdalen, S. Wenner, E.A. Mørtzell, R. Holmestad, T. Saito, J. Røyset, and O. Reiso: *Mater. Sci. Forum*, 2017, vol. 877, pp. 461–70.
- O. Reiso, N. Ryum, and J. Strid: *Metall. Trans. A*, 1993, vol. 24A, pp. 2629–41.
- G. Sha, K. O'Reilly, and B. Cantor: *Mater. Sci. Forum*, 2006, vol. 519–21, pp. 1721–26.
- H. Tanihata, T. Sugawara, K. Matsuda, and S. Ikeno: *J. Mater. Sci.*, 1999, vol. 34, pp. 1205–10.
- M.S. Remøe, K. Marthinsen, I. Westermann, K. Pedersen, J. Røyset, and C. Marioara: *Mater. Sci. Eng. A*, 2017, vol. 693, pp. 60–72.
- T. Furu, N. Telioui, C. Behrens, J. Hasenclever, and P. Schaffer: *Proceedings of the 12 ICAA*, 2010, pp. 282–89.
- M. Mihara, C.D. Marioara, S.J. Andersen, R. Holmestad, E. Kobayashi, and T. Sato: *Mater. Sci. Eng. A*, 2016, vol. 658, pp. 91–98.
- L. Kovarik, S.A. Court, H.L. Fraser, and M.J. Mills: *Acta Mater.*, 2008, vol. 56, pp. 4804–15.
- J.A. Mir, R. Clough, R. MacInnes, C. Gough, R. Plackett, I. Shipsey, H. Sawada, I. MacLaren, R. Ballabriga, D. Maneuski, V. O'Shea, D. McGrouther, and A.I. Kirkland: *Ultramicroscopy*, 2017, vol. 182, pp. 44–53.
- J.S. Barnard, D.N. Johnstone, and P.A. Midgley: *Ultramicroscopy*, 2017, vol. 174, pp. 79–88.
- J. Schindelin, I. Arganda-Carreras, E. Frise, V. Kaynig, M. Longair, T. Pietzsch, S. Preibisch, C. Rueden, S. Saalfeld, B. Schmid, J.Y. Tinevez, D.J. White, V. Hartenstein, K. Eliceiri, P. Tomancak, and A. Cardona: *Nat Methods*, 2012, vol. 9, p. 676.
- H.W. Ánes: Metallography-notebooks. https://github.com/hakonanes/metallography-notebooks/blob/master/particle_size_distribution_from_bse_image/particle_size_distribution_from_bse_image.i_pynb, (accessed June 22, 2020).
- S.J. Andersen: *Metall. Mater. Trans. A.*, 1995, vol. 26A, pp. 1931–37.
- M. Cooper: *Acta Crystallogr. A*, 1967, vol. 23, pp. 1106–07.
- O. Madelung, U. Rössler, and M. Schulz: *Non-Tetrahedrally Bonded Elements and Binary Compounds I*, Springer, 2005, pp. 1–4.
- H. Tvedt, C.D. Marioara, E. Thronsen, C. Hell, S.J. Andersen, and R. Holmestad: *Ultramicroscopy*, 2022, vol. 236, p. 113493.
- F. de la Peña, E. Prestat, V.T. Fauske, P. Burdet, T. Furnival, P. Jokubauskas, M. Nord, T. Ostasevicius, J. Lähnemann, K.E. MacArthur, D.N. Johnstone, M. Sarahan, J. Taillon, T. Aarholt, pquinn-dls, V. Mignunov, A. Eljarrat, J. Caron, T. Poon, S. Maz-zucco, B. Martineau, S. Somnath, T. Slater, C. Francis, action-s-user, M. Walls, N. Tappy, N. Cautaerts, F. Winkler, and G. Donval: <https://doi.org/10.5281/ZENODO.4923970>.
- D.N. Johnstone, P. Crout, M. Nord, J. Laulainen, S. Høgås, EirikOpheim, B. Martineau, C. Francis, T. Bergh, E. Prestat, S. Smeets, andrew-ross1, S. Collins, I. Hjorth, Mohsen, T. Furnival, D. Jannis, N. Cautaerts, E. Jacobsen, AndrewHerzing, T. Poon, H.W. Ánes, J. Morzy, S. Huang, phillipcrout, T. Doherty, affan-qbal, T. Ostasevicius, mvonlany, and R. Tovey: 2021.
- S. van der Walt, J.L. Schönberger, J. Nunez-Iglesias, F. Boulogne, J.D. Warner, N. Yager, E. Gouillart, T. Yu, and the scikit-image contributors: *PeerJ*, 2014, vol. 2, p. e453.
- S.R. Sternberg: *Computer*, 1983, vol. 16, pp. 22–34.
- Z. Gw, R. We, and L. Sa: *J Histochem Cytochem*, 1977, vol. 25, pp. 741–53.
- H.G. Merkus: *Particle Size Measurements*, 2009, pp. 13–42.
- D.D. Lee and H.S. Seung: *Nature*, 1999, vol. 401, pp. 788–91.
- J.K. Sunde, C.D. Marioara, A.T.J. van Helvoort, and R. Holmestad: *Mater. Charact.*, 2018, vol. 142, pp. 458–69.
- E. Linardi, R. Haddad, and L. Lanzani: *Procedia Mater. Sci.*, 2012, vol. 1, pp. 550–57.
- M. Torsæter, F.J.H. Ehlers, C.D. Marioara, S.J. Andersen, and R. Holmestad: *Philos. Mag.*, 2012, vol. 92, pp. 3833–56.
- C.D. Marioara, S.J. Andersen, J. Røyset, O. Reiso, S. Gulbrandsen-Dahl, T.E. Nicolaisen, I.E. Opheim, J.F. Helgaker, and R. Holmestad: *Metall. Mater. Trans. A*, 2014, vol. 45A, pp. 2938–49.
- M. Werinos, H. Antrekowitsch, T. Ebner, R. Prillhofer, P.J. Uggowitzer, and S. Pogatscher: *Mater. Des.*, 2016, vol. 107, pp. 257–68.
- J.D. Embury, A. Deschamps, and Y. Brechet: *Scripta Mater.*, 2003, vol. 49, pp. 927–32.
- T. Saito, S. Muraishi, C.D. Marioara, S.J. Andersen, J. Røyset, and R. Holmestad: *Metall. Mater. Trans. A*, 2013, vol. 44A, pp. 4124–35.
- K. Teichmann, C.D. Marioara, S.J. Andersen, K.O. Pedersen, S. Gulbrandsen-Dahl, M. Kolar, R. Holmestad, and K. Marthinsen: *Philos Mag*, 2011, vol. 91, pp. 3744–54.
- K. Teichmann, C.D. Marioara, S.J. Andersen, and K. Marthinsen: *Metall. Mater. Trans. A.*, 2012, vol. 43A, pp. 4006–14.
- W.J. Poole, X. Wang, D.J. Lloyd, and J.D. Embury: *Philos. Mag.*, 2005, vol. 85, pp. 3113–35.

Publisher's Note Springer Nature remains neutral with regard to jurisdictional claims in published maps and institutional affiliations.